INTERNATIONAL JOURNAL FOR NUMERICAL METHODS IN FLUIDS
Int. J. Numer. Meth. Fluids 2004; **45**:1209–1233 (DOI: 10.1002/fld.738)

Development of a convection–diffusion-reaction magnetohydrodynamic solver on non-staggered grids

Tony W. H. Sheu*,†,‡ and R. K. Lin§

Department of Engineering Science and Ocean Engineering, National Taiwan University, No. 1, Sec. 4, Roosevelt Road, Taipei, Taiwan, Republic of China

SUMMARY

This paper presents a convection–diffusion-reaction (CDR) model for solving magnetic induction equations and incompressible Navier–Stokes equations. For purposes of increasing the prediction accuracy, the general solution to the one-dimensional constant-coefficient CDR equation is employed. For purposes of extending this discrete formulation to two-dimensional analysis, the alternating direction implicit solution algorithm is applied. Numerical tests that are amenable to analytic solutions were performed in order to validate the proposed scheme. Results show good agreement with the analytic solutions and high rate of convergence. Like many magnetohydrodynamic studies, the Hartmann–Poiseuille problem is considered as a benchmark test to validate the code. Copyright © 2004 John Wiley & Sons, Ltd.

KEY WORDS: convection–diffusion-reaction; magnetic induction equations; incompressible; Navier–Stokes; Hartmann–Poiseuille

1. INTRODUCTION

Computational magnetohydrodynamics (MHD) has been the subject of intensive research for investigating the motion of conducting fluid flow subject to a magnetic field [1]. Analysis of this class of flows involves solving Maxwell equations of electrodynamics. The conducting fluid flow can induce electric current and interact with the magnetic field. This interaction in turn produces Lorentz force on the fluid and can greatly change the flow behaviour. The complex coupling between hydrodynamic and magnetic fields may result in sharply varying magnetic field and current sheet [2]. Another distinct feature that is hardly seen in the non-conducting flow equations is the formation of Alfven wave, which can possibly lead to hydrodynamic instability [3]. In this paper, we consider incompressible MHD equations, which

*Correspondence to: Tony W. H. Sheu, Department of Engineering Science and Ocean Engineering, National Taiwan University, No. 1, Sec. 4, Roosevelt Road, Taipei, Taiwan, Republic of China.
†E-mail: twhsheu@ntu.edu.tw
‡Professor.
§Ph.D. Candidate.

Contract/grant sponsor: National Science Council of the Republic of China; contract/grant number: NSC 88-2611-E-002-025

Published online 25 May 2004

Received 21 June 2003
Revised 22 January 2004

are computationally challenging and are technologically important in areas of metal casting, nuclear cooling, and deposition processes. In addition, MHD plays an essential role in the design of electromagnetic pumps, induction furnaces, and electrolysis cells.

In the simulation of coupling between flow and magnetic fields, one can resort to methods using the magnetic flux density as the working magnetic variable or to others using the vector potential in conjunction with its associated scalar potential [4]. One can refer [5] for an overview of the vector potential methods. Choosing between two classes of formulation is not a trivial task, and we find no definite guidelines in the literature. In the present paper, we employ the primitive variable approach for solving the magnetic and hydrodynamic field equations on non-staggered grids.

The remainder of the paper is organized in eight sections. In Section 2, hydrodynamic equations which are coupled with the Maxwell's equations and Ohm's law for electrodynamics are presented. In Section 3, the finite difference scheme is developed for the solution of magnetic equation in the specified flow. The novelty of the present scheme is the use of nodally exact convection–diffusion-reaction solution in each alternating direction implicit (ADI) sweep. Section 4 is devoted to the Fourier (or von Neumann) stability analysis of the proposed scheme. In Section 5, the co-located grid approach is employed in the simulation of incompressible Navier–Stokes equations in primitive variables. In Section 6, several benchmark problems that are amenable to analytic solutions are solved to justify the proposed convection–diffusion-reaction model. The test problem in Section 7 was performed to validate the incompressible magnetohydrodynamic code. Primary conclusions are summarized in the last section.

2. WORKING EQUATION

Analysis of electromagnetics in liquid metals involves solving the Maxwell equations for the non-existence of a magnetic monopole, Faraday's law, pre-Maxwell Ampere's law, and Gauss's law, respectively [4]:

$$\nabla \cdot \mathbf{B} = 0 \tag{1}$$

$$\nabla \times \mathbf{E} = -\frac{\partial \mathbf{B}}{\partial t} \tag{2}$$

$$\nabla \times \mathbf{B} = \mu_0 \mathbf{J} \tag{3}$$

$$\nabla \cdot \mathbf{D} = q \tag{4}$$

In the above, $\mathbf{B}$ denotes the magnetic induction (flux density), $\mathbf{H}$ the magnetic field density, $\mathbf{D}$ the electric displacement (flux density), $\mathbf{E}$ the electric field, $\mathbf{J}$ ($\equiv \sigma \mathbf{E}$) the electric current density, and q the electric charge density. Note that Equation (3) is derived under the assumption that the displacement current $\partial \mathbf{D}/\partial t$ is negligibly small in comparison with other terms in the following Ampere's law [6]:

$$\nabla \times \mathbf{H} = \mathbf{J} + \frac{\partial \mathbf{D}}{\partial t} \tag{5}$$

Considering a free space (or a non-magnetizable and non-polarizable) electromagnetic medium, the above system of Maxwell's equations is supplemented linearly with $\mathbf{H} = \mathbf{B}/\mu_0$ and $\mathbf{E} = \mathbf{D}/\varepsilon_0$. Two constants shown above are known as the free-space magnetic permeability μ_0 ($\equiv 4\pi \times 10^{-7}$ Hs/m) and the free-space electric permittivity ε_0 ($\equiv 8.854 \times 10^{-12}$ F/m).

One constitutive law is needed to characterize the ability of the investigated conducting fluid to transport electric charges under the influence of applied electric field. The employed Ohm's law is given below for relating the electric current density $\mathbf{J}$ to the electric field:

$$\mathbf{J} = \sigma(\mathbf{E} + \mathbf{u} \times \mathbf{B}) \tag{6}$$

In the above, σ is the electric conductivity of the material (or $1/\sigma$ as the electric resistivity). Note that the above constitutive equation is derived under the assumption of neglecting convection current $q\mathbf{u}$ (or making a quasi-neutrality hypothesis) in a system characterized by the non-relativistic motion having a velocity $\mathbf{u}$ [6].

Since $\mathbf{B}$ will be considered as the principal magnetic field variable, we perform the curl operator on each term in the above Ohm's law. The following magnetic induction equation is derived in lieu of Equations (2) and (3):

$$\frac{\partial \mathbf{B}}{\partial t} = \nabla \times (\mathbf{u} \times \mathbf{B}) + \frac{1}{\sigma\mu}\nabla^2 \mathbf{B} \tag{7}$$

The above equation enlightens the coupling of hydrodynamic and electromagnetic two fields. In the presence of gravitational force $\rho\mathbf{g}$, incompressible Navier–Stokes equations, subject to a divergence-free velocity constraint condition, are expressed in the form

$$\nabla \cdot \mathbf{u} = 0 \tag{8}$$

$$\frac{\partial \mathbf{u}}{\partial t} + (\mathbf{u} \cdot \nabla)\mathbf{u} = -\frac{1}{\rho}\nabla p + \nu_f \nabla^2 \mathbf{u} + \mathbf{F} \tag{9}$$

In Equation (9), ν_f represents the kinematic viscosity, ρ the density of the conducting fluid, p the pressure, and $\mathbf{F}$ the total body force vector ($\mathbf{F} = \mathbf{F}_{em} + \mathbf{F}_{ext}$). For non-magnetizable and non-polarizable media, the electric contribution can be neglected in comparison with the magnetic term. As a result, $\mathbf{F}_{em}$ consists of only the Lorentz's force $\mathbf{F}_{em} = (1/\rho)\mathbf{J} \times \mathbf{B}$. We consider for simplicity the case without system rotation and thermal buoyancy. The external body force vector can, thus, be expressed as $\mathbf{F}_{ext} = \mathbf{g}$. In other words, $\mathbf{F} = \mathbf{g} + (1/\rho)\mathbf{J} \times \mathbf{B}$.

The hydrodynamic equations (8) and (9) and the conservation equations for $\mathbf{B}$ constitute the differential system for modelling the incompressible conducting flow motion in a magnetic field. For purposes of general applications, we shall normalize the hydro-magnetic field equations (2)–(9) through the user's chosen characteristic length L and the characteristic velocity u_∞ as follows: $(x^*, y^*) = (x/L, y/L)$, $(u^*, v^*) = (u/u_\infty, v/u_\infty)$, $t^* = t/(L/u_\infty)$, and $p^* = p/\rho u_\infty$. In regard to $\mathbf{B} = (B_x, B_y)$, it is scaled by B_0 to obtain $(B_x^*, B_y^*) = (B_x/B_0, B_y/B_0)$. Omitting the superscript '*' for the sake of simplicity, the dimensionless equations for the conducting fluid flow in the presence of an externally specified B_0 are derived as

$$\frac{\partial u}{\partial x} + \frac{\partial v}{\partial y} = 0 \tag{10}$$

$$\frac{\partial u}{\partial t}+u\frac{\partial u}{\partial x}+v\frac{\partial u}{\partial y}=-\frac{\partial p}{\partial x}+\frac{1}{Re_{\mathrm{f}}}\left(\frac{\partial^2 u}{\partial x^2}+\frac{\partial^2 u}{\partial y^2}\right)+\frac{H_a^2}{Re_{\mathrm{f}}Re_{\mathrm{m}}}B_y\left(\frac{\partial B_x}{\partial y}-\frac{\partial B_y}{\partial x}\right) \tag{11}$$

$$\frac{\partial v}{\partial t}+u\frac{\partial v}{\partial x}+v\frac{\partial v}{\partial y}=-\frac{\partial p}{\partial y}+\frac{1}{Re_{\mathrm{f}}}\left(\frac{\partial^2 v}{\partial x^2}+\frac{\partial^2 v}{\partial y^2}\right)-\frac{H_a^2}{Re_{\mathrm{f}}Re_{\mathrm{m}}}B_x\left(\frac{\partial B_x}{\partial y}-\frac{\partial B_y}{\partial x}\right) \tag{12}$$

$$\frac{\partial B_x}{\partial t}+u\frac{\partial B_x}{\partial x}+v\frac{\partial B_x}{\partial y}-\frac{1}{Re_{\mathrm{m}}}\left(\frac{\partial^2 B_x}{\partial x^2}+\frac{\partial^2 B_x}{\partial y^2}\right)+\frac{\partial v}{\partial y}B_x=\frac{\partial u}{\partial y}B_y \tag{13}$$

$$\frac{\partial B_y}{\partial t}+u\frac{\partial B_y}{\partial x}+v\frac{\partial B_y}{\partial y}-\frac{1}{Re_{\mathrm{m}}}\left(\frac{\partial^2 B_y}{\partial x^2}+\frac{\partial^2 B_y}{\partial y^2}\right)+\frac{\partial u}{\partial x}B_y=\frac{\partial v}{\partial x}B_x \tag{14}$$

Note that the production term $(\mathbf{B}\cdot\nabla)\mathbf{u}$ in the above MHD equations results from the stretched flux lines. As for $1/Re_{\mathrm{m}}\nabla^2\mathbf{B}$, it represents the magnetic diffusion. In the above, three key dimensionless parameters are known as the fluid Reynolds number $Re_{\mathrm{f}}(\equiv Lu_\infty/\nu_{\mathrm{f}})$, the magnetic Reynolds number $Re_{\mathrm{m}}(\equiv Lu_\infty/\eta)$, and the Hartmann number $H_a(\equiv\sigma B_0^2L^2/\rho\nu_{\mathrm{f}})$. The square of H_a is the ratio of the Lorentz force to the viscous force [7]. By analogy with ν_{f}, η in the definition of magnetic Reynolds number is called the magnetic diffusion and is defined as $\eta=1/\sigma\mu$.

The material property $Re_{\mathrm{m}}/Re_{\mathrm{f}}(\equiv\nu_{\mathrm{f}}/\eta)$ for the typical liquid metal (e.g. mercury or gallium) is around 10^{-6}. The consequence of such a small material property is that the chosen viscous diffusion time scale differs considerably from the magnetic diffusion time scale. This implies that if the time scale is sufficient to resolve the magnetic diffusive time scale, tens or even hundreds of millions of time steps are needed to cover one viscous diffusive time scale. Since Re_{m} is so small, we can expand the magnetic field variable with respect to the externally applied $\mathbf{B}_0$ and neglect higher order terms to render $\mathbf{B}$ as the sum of $\mathbf{B}_0$ and the induced field $Re_{\mathrm{m}}\mathbf{b}$. The induction equation given in (7) then reduces to the time-independent elliptic equation $\nabla\times(\mathbf{U}\times\mathbf{B}_0)+\nabla^2\mathbf{b}=0$. The remaining time derivative terms in the coupled MHD equations are $\partial u/\partial t$ and $\partial v/\partial t$. One now can simply take the viscous diffusive time scale into consideration by choosing Δt appropriate to approximate $\partial\mathbf{u}/\partial t$ shown in the momentum equations. For more details about this approach, one can refer to the work of Hollerbach and Skinner [8].

3. NUMERICAL MODEL

As Equations (11) and (12) show, the magnetic induction can cause the conducting fluid flow to accelerate. For this reason, we were motivated to develop an accurate scheme to simulate the magnetic induction equations in the conducting flow field $\mathbf{u}=(U,V)$. The prototype equation for (13) and (14), subject to the Dirichlet-type boundary condition, in a constant velocity field (u,v) takes the following form:

$$\phi_t+U\phi_x+V\phi_y-K(\phi_{xx}+\phi_{yy})+C\phi=S \tag{15}$$

The diffusion coefficient K and the reaction coefficient C are assumed to be constant.

For purposes of computational efficiency, we apply the ADI scheme of Peaceman and Rachford [9] to obtain ϕ iteratively through the two steps given below

Predictor step:

$$\phi_t^* + U\phi_x^* - K\phi_{xx}^* + C\phi^* = S^* - V\phi_y^n + K\phi_{yy}^n \tag{16}$$

Corrector step:

$$\phi_t^{n+1} + V\phi_y^{n+1} - K\phi_{yy}^{n+1} + C\phi^{n+1} = S^{n+1} - U\phi_x^* + K\phi_{xx}^* \tag{17}$$

In view of the above two inhomogeneous convection–diffusion-reaction equations, the key to success in solving Equation (15) is the discretization of the following model equation:

$$\phi_t + a\phi_x - \mu\phi_{xx} + c\phi = f \tag{18}$$

where f is assumed to be constant to facilitate the scheme development.

Within this semi-discretization framework, ϕ_t is approximated by conducting the Taylor series expansion of ϕ with respect to t

$$\phi^{n+1} = \phi^n + \Delta t\phi_t^n + \frac{(\Delta t)^2}{2!}\phi_{tt}^n + \frac{(\Delta t)^3}{3!}\phi_{ttt}^n + \frac{(\Delta t)^4}{4!}\phi_{tttt}^n + \cdots + \text{H.O.T.} \tag{19}$$

Depending on the number of truncated terms on the right-hand side of (19), the temporal accuracy varies accordingly. In this study, we choose the following approximation:

$$\phi^{n+1} = \phi^n + \Delta t\phi_t^n + \frac{(\Delta t)^2}{2}\phi_{tt}^n \tag{20}$$

The expression for ϕ_t^n shown in (20) can be directly obtained from Equation (18) as

$$\phi_t^n = f^n - a\phi_x^n + \mu\phi_{xx}^n - c\phi^n \tag{21}$$

As to ϕ_{tt}^n, it is approximated by virtue of

$$\phi_{tt}^n = \left(\frac{\phi_t^{n+1} - \phi_t^n}{\Delta t}\right) \tag{22}$$

Substituting Equation (21) for ϕ_t^n and Equation (22) for ϕ_{tt}^n into Equation (20), the following convection–diffusion-reaction equation is obtained:

$$\bar{a}\phi_x^{n+1} - \bar{\mu}\phi_{xx}^{n+1} + \bar{c}\phi^{n+1} = \bar{f} \tag{23}$$

where $(\bar{a}, \bar{\mu}, \bar{c}, \bar{f}) = (a\Delta t, \mu\Delta t, c\Delta t + 2, f\Delta t + 2\phi^n + \phi_t^n)$. As Equation (23) reveals, the key to success in the current calculation lies in the analysis of the following one-dimensional equation:

$$\bar{u}^*\phi_x - \bar{\mu}^*\phi_{xx} + \bar{c}^*\phi = \bar{f}^* \tag{24}$$

For illustrative purpose, $\bar{f}^*$ is assumed to be a known constant throughout. To increase the prediction accuracy, our strategy is to employ the general solution for Equation (24):

$$\phi(x) = c_1 e^{\lambda_1 x} + c_2 e^{\lambda_2 x} + \frac{\bar{f}^*}{\bar{c}^*} \tag{25}$$

In the above, c_1 and c_2 are constants. Substituting Equation (25) into Equation (24), we are led to have $(\lambda_1, \lambda_2) = (\frac{\bar{a}^* + \sqrt{\bar{a}^{*2} + 4\bar{c}^*\bar{\mu}^*}}{2\bar{\mu}^*}, \frac{\bar{a}^* - \sqrt{\bar{a}^{*2} + 4\bar{c}^*\bar{\mu}^*}}{2\bar{\mu}^*})$. With the exception of convective terms, other terms shown in (24) are approximated by the centre-like scheme. Therefore, the discrete equation at an interior node j can be expressed as

$$\left(-\frac{\bar{a}^*}{2h} - \frac{m}{h^2} + \frac{\bar{c}^*}{6}\right)\phi_{j-1} + 2\left(\frac{m}{h^2} + \frac{\bar{c}^*}{3}\right)\phi_j + \left(\frac{\bar{a}^*}{2h} - \frac{m}{h^2} + \frac{\bar{c}^*}{6}\right)\phi_{j+1} = \bar{f}^* \tag{26}$$

In the above, h is the uniform grid size. We proceed to substitute the exact solutions $\phi_j = c_1 e^{\lambda_1 x_j} + c_2 e^{\lambda_2 x_j} + \bar{f}^*/\bar{c}^*$, $\phi_{j+1} = c_1 e^{\lambda_1 h} e^{\lambda_1 x_j} + c_2 e^{\lambda_2 h} e^{\lambda_2 x_j} + \bar{f}^*/\bar{c}^*$, and $\phi_{j-1} = c_1 e^{-\lambda_1 h} e^{\lambda_1 x_j} + c_2 e^{-\lambda_2 h} e^{\lambda_2 x_j} + \bar{f}^*/\bar{c}^*$ into Equation (26) and derive m analytically as [10]

$$m = h^2 \left\{ \frac{\frac{\bar{c}^*}{3} + \frac{\bar{c}^*}{6}\cosh(\overline{\lambda_1})\cosh(\overline{\lambda_2}) + \frac{\bar{a}^*}{2h}\sinh(\overline{\lambda_1})\cosh(\overline{\lambda_2})}{\cosh(\overline{\lambda_1})\cosh(\overline{\lambda_2}) - 1} \right\} \tag{27}$$

where $(\overline{\lambda_1}, \overline{\lambda_2}) = (\bar{a}^* h/2\bar{\mu}^*, [(\bar{a}^* h/2\bar{\mu}^*)^2 + \bar{c}^* h^2/\bar{\mu}^*]^{1/2})$. Note that the numerical error stems solely from the approximation of $\bar{f}^*$.

4. FUNDAMENTAL STUDY ON THE DISCRETIZATION SCHEME

As a key success in the discretization of (15), we explore both dissipation and dispersion characters of the underlying scheme at the homogeneous (or $f = 0$) condition for Equation (18). Given the initial condition of $\phi(x, t = 0) = \exp(\mathrm{i}k_m x)$, Equation (18) is amenable to the exact solution given by

$$\phi(x, t) = \exp[-(\mu k_m^2 + c)t] \exp[\mathrm{i}k_m(x - at)] \tag{28}$$

where k_m denotes the wave-number. With $h(\equiv \Delta x)$ as the mesh size and Δt as the time increment, the discrete equation for (18) is as follows:

$$\begin{aligned} &A_1\phi_{j-1}^{n+1} + A_2\phi_j^{n+1} + A_3\phi_{j+1}^{n+1} \\ &\quad = B_1\phi_{j-4}^n + B_2\phi_{j-3}^n + B_3\phi_{j-2}^n + B_4\phi_{j-1}^n + B_5\phi_j^n + B_6\phi_{j+1}^n + B_7\phi_{j+2}^n + B_8\phi_{j+3}^n \end{aligned} \tag{29}$$

In the above, A_1, A_2, A_3 are expressed in terms of $v = a\Delta t/h$ as

$$A_1 = -\frac{\bar{m}}{h^2} - \frac{v}{2} + \frac{vR + 2}{6} \tag{30}$$

$$A_2 = 2\left(\frac{\bar{m}}{h^2} + \frac{vR+2}{3}\right) \tag{31}$$

$$A_3 = -\frac{\bar{m}}{h^2} + \frac{v}{2} + \frac{vR+2}{6} \tag{32}$$

As for B_1–B_8, they are detailed in Appendix A. Defining $Pe = ah/\mu$ and $R = ch/a$, $\bar{m}$ shown in Equations (30)–(32) can be expressed as

$$\bar{m} = h^2 \left\{ \frac{\frac{vR+2}{3} + \frac{vR+2}{6}\cosh(\overline{\lambda_1}^*)\cosh(\overline{\lambda_2}^*) + \frac{v}{2}\sinh(\overline{\lambda_1}^*)\cosh(\overline{\lambda_2}^*)}{\cosh(\overline{\lambda_1}^*)\cosh(\overline{\lambda_2}^*) - 1} \right\} \tag{33}$$

where

$$\overline{\lambda_1}^* = \frac{Pe}{2} \tag{34}$$

$$\overline{\lambda_2}^* = \left[\left(\frac{Pe}{2}\right)^2 + Pe\left(\frac{2}{v} + R\right)\right]^{1/2} \tag{35}$$

Owing to the possible amplitude and phase errors, the exact solution to the finite–difference Equation (29) is assumed to take the following form:

$$\phi(x,t) = \exp\left[-(\mu k_m^2 + c)\frac{k_r}{\alpha^2}t\right]\exp\left[\mathrm{i}k_m\left(x - a\frac{k_i}{\alpha}t\right)\right] \tag{36}$$

where the modified wave-number is expressed as $\alpha = k_m h$. Dispersion analysis is made by substituting ϕ_j and $\phi_{j\pm1}$, which are obtained from Equation (36), into Equation (29). After some algebra, k_r and k_i, which are the measures of amplitude and phase errors, are derived as

$$k_r = -\frac{P}{v((1/Pe) + (R/\alpha^2))} \tag{37}$$

$$k_i = -\frac{Q}{v} \tag{38}$$

where

$$P = \ln\left\{\sqrt{\left[\frac{F_1X - F_2Y}{X^2+Y^2}\right]^2 + \left[\frac{F_1Y + F_2X}{X^2+Y^2}\right]^2}\right\} \tag{39}$$

$$Q = \tan^{-1}\left\{\frac{F_1Y + F_2X}{F_1X - F_2Y}\right\} \tag{40}$$

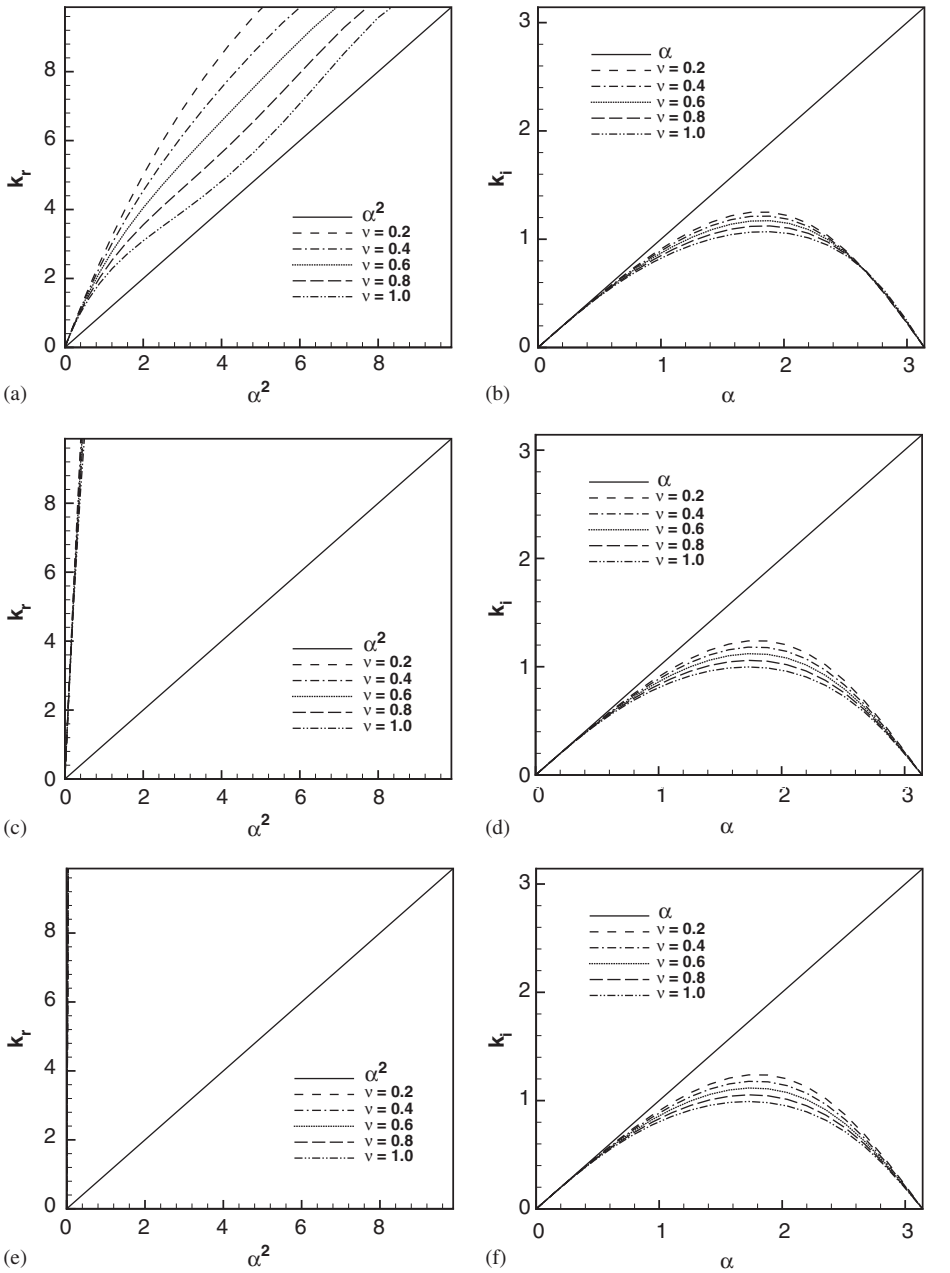

Figure 1. Plots of k_r and k_i against $R = 0$, Pe and v at different Peclet numbers: (a)–(b) $Pe = 10$; (c)–(d) $Pe = 100$; and (e)–(f) $Pe = 1000$.

$$X = (A_1 + A_3)\cos\alpha + A_2 \tag{41}$$

$$Y = (A_1 - A_3)\sin\alpha \tag{42}$$

In the above, F_1 and F_2 are expressed as

$$F_1 = B_1\cos 4\alpha + (B_2 + B_8)\cos 3\alpha + (B_3 + B_7)\cos 2\alpha + (B_4 + B_6)\cos\alpha + B_5 \tag{43}$$

$$F_2 = -[B_1\sin 4\alpha + (B_2 - B_8)\sin 3\alpha + (B_3 - B_7)\sin 2\alpha + (B_4 - B_6)\sin\alpha] \tag{44}$$

We plot in Figure 1 the distributions of k_r and k_i against Pe, R and v. It is seen that k_r and k_i agree perfectly with α^2 and α, respectively, in the low modified wave-number range. The higher the modified wave-number, the less satisfactory is the performance of the scheme.

5. FLOW CALCULATION ON NON-STAGGERED GRIDS

Centre differencing of $\partial p/\partial x$ and $\partial p/\partial y$ in (11) and (12) has been known to be the origin to produce spurious even-odd oscillations on non-staggered grids [11–13] For this reason, we attempt to eliminate the erroneous checkerboarding pressure on co-located grids. Since p_j in the calculation of $\nabla p|_j$ is crucial to the avoidance of even–odd unphysical oscillations, we are not allowed to compute $\partial p/\partial x|_j$, for example, directly from the conventional centred schemes. Instead, $F_j(\equiv h\partial p/\partial x|_j)$ is implicitly related with its two adjacent values $F_{j\pm1}$ as follows:

$$\begin{aligned}\alpha_0 F_{j+1} + \beta_0 F_j + \gamma_0 F_{j-1} = {} & a_0(p_{j+2} - p_{j+1}) + b_0(p_{j+1} - p_j) \\ & + c_0(p_j - p_{j-1}) + d_0(p_{j-1} - p_{j-2})\end{aligned} \tag{45}$$

The above implicit equation, while making the calculation of pressure gradient more expensive, involves p_j itself and, thus, makes the calculation of $\partial p/\partial x|_j$ physically meaningful.

Expansion of $F_{j\pm1}$ and $p_{j\pm1}$, $p_{j\pm2}$ in Taylor series with respect to F_j and p_j, respectively, renders the same number of algebraic equations as the unknown coefficients shown in Equation (45). On physical grounds, it is rational to set $\alpha_0 = \gamma_0$ *a priori* in view of the elliptic nature of the pressure. Thus, coefficients shown above are uniquely determined as $\alpha_0 = \gamma_0 = \frac{1}{5}$, $\beta_0 = \frac{3}{5}$, $a_0 = d_0 = \frac{1}{60}$ and $b_0 = c_0 = \frac{29}{60}$. To obtain the discrete equations for F at nodes immediately adjacent to the boundary points, it is legitimate to specify $d_0 = 0$ and $a_0 = 0$ at nodes next to the left and right boundaries, respectively. By performing the Taylor series expansion as that mentioned earlier, we are led to have $(\alpha_0, \beta_0, \gamma_0, a_0, b_0, c_0, d_0) = (\frac{3}{10}, \frac{3}{5}, \frac{1}{10}, \frac{1}{30}, \frac{19}{30}, \frac{1}{3}, 0)$ and $(\frac{1}{10}, \frac{3}{5}, \frac{3}{10}, 0, \frac{1}{3}, \frac{19}{30}, \frac{1}{30})$ at nodes next to the left and right boundaries, respectively.

The quality of the present scheme for Equation (15) depends solely on how accurately the spatial derivatives in the source term are computed. To provide a physically rational approximation of ϕ_x, for example, we apply the following approximated

expressions:

$$\mathbf{u}>0: \quad \phi_x|_j = \frac{1}{60h}(\phi_{j-4} - 8\phi_{j-3} + 30\phi_{j-2} - 80\phi_{j-1} + 35\phi_j + 24\phi_{j+1} - 2\phi_{j+2}) \tag{46}$$

$$\mathbf{u}<0: \quad \phi_x|_j = \frac{1}{60h}(2\phi_{j-2} - 24\phi_{j-1} - 35\phi_j + 80\phi_{j+1} - 30\phi_{j+2} + 8\phi_{j+3} - \phi_{j+4}) \tag{47}$$

Note that the nodal values upstream of j should be favourably considered for the convection dominated case. At nodes next to the most left and right interior points (or cases with $j=1$ and $j_{\max}$), we apply the following expressions:

$$\phi_x|_{j=1} = \frac{-1}{60h}(147\phi_j - 360\phi_{j+1} + 450\phi_{j+2} - 400\phi_{j+3} + 225\phi_{j+4} - 72\phi_{j+5} + 10\phi_{j+6}) \tag{48}$$

$$\phi_x|_{j=j_{\max}} = \frac{1}{60h}(147\phi_j - 360\phi_{j-1} + 450\phi_{j-2} - 400\phi_{j-3} + 225\phi_{j-4} - 72\phi_{j-5} + 10\phi_{j-6}) \tag{49}$$

On physical grounds, the second derivative term for ϕ_{xx} is approximated by employing the following sixth-order accurate expression:

$$\phi_{xx}|_j = \frac{1}{180h^2}(2\phi_{j-3} - 27\phi_{j-2} + 270\phi_{j-1} - 490\phi_j + 270\phi_{j+1} - 27\phi_{j+2} + 2\phi_{j+3}) \tag{50}$$

At nodes adjacent to the two end boundaries, we can approximate ϕ_{xx} using the equations given below

$$\phi_{xx}|_{j=1} = \frac{1}{180h^2}(812\phi_j - 3132\phi_{j+1} + 5265\phi_{j+2} - 5080\phi_{j+3} + 2970\phi_{j+4} - 972\phi_{j+5} + 137\phi_{j+6}) \tag{51}$$

$$\phi_{xx}|_{j=j_{\max}} = \frac{1}{180h^2}(812\phi_j - 3132\phi_{j-1} + 5265\phi_{j-2} - 5080\phi_{j-3} + 2970\phi_{j-4} - 972\phi_{j-5} + 137\phi_{j-6}) \tag{52}$$

The cavity flow driven by a constant upper lid velocity u_∞ will be considered to suppress oscillatory pressure solutions on co-located grids. With ℓ as the characteristic length, u_{lid} the characteristic velocity, and ρ the fluid viscosity, the Reynolds number $Re(\equiv \rho u_{\text{lid}}\ell/\mu)$ under investigation is 3000. It is essential to continuously refine the mesh to obtain a grid independent solution. We plot the mid-plane velocity profiles $u(0.5, y)$ and $v(x, 0.5)$ in Figure 2 and compare them with the steady-state benchmark solution obtained by Ghia [14].

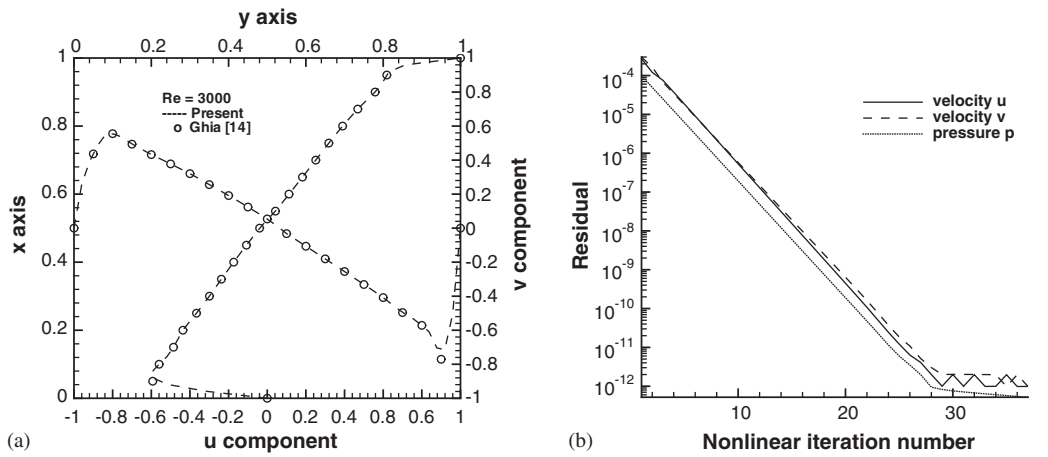

Figure 2. (a) The computed velocity profiles $u(x, 0.5)$ and $v(0.5, y)$ for the case considered at $Re = 3000$; and (b) the convergence history for the case investigated in the 40×40 discretized domain.

The good agreement between two solutions validates the co-located scheme applied to the incompressible viscous flow simulation.

6. VALIDATION STUDIES

We will consider firstly the homogeneous steady constant-coefficient convection–diffusion equation in $0 \leqslant x, y \leqslant 1$:

$$a\phi_x + b\phi_y = k(\phi_{xx} + \phi_{yy}) \tag{53}$$

Given the boundary values of $\phi(1, y) = \phi(x, 1) = 0$, $\phi(x, 0) = (1 - \exp[(x - 1)a/k])/(1 - \exp(-a/k))$ and $\phi(0, y) = (1 - \exp[(y - 1)b/k])/(1 - \exp(-b/k))$, the exact solution to the above viscous Burgers equation takes the following form [15]:

$$\phi(x, y) = \left\{ \frac{1 - \exp[(x - 1)a/k]}{1 - \exp(-a/k)} \right\} \left\{ \frac{1 - \exp[(y - 1)b/k]}{1 - \exp(-b/k)} \right\} \tag{54}$$

Computations were carried out at $k = 1$, different velocities ($a = b = 1, 10$, and 100) and mesh sizes ($\Delta x = \Delta y = \frac{1}{10}, \frac{1}{20}, \frac{1}{40}, \frac{1}{80}$ and $\frac{1}{160}$). For each case, the computed error was cast in its L_2-norm form. This was followed by plotting in Figure 3 the value of $\log(\mathrm{err}_1/\mathrm{err}_2)$ against $\log(h_1/h_2)$, where two errors err_1 and err_2 are obtained at consecutively refined mesh sizes h_1 and h_2, to obtain the scheme's rate of convergence. Good agreement with the benchmark results and fast convergence to the analytic solution are demonstrated.

We then solve for the steady-state variable-coefficient CDR model equation in the unit square $0 \leqslant x, y \leqslant 1$. Under the conditions $(a, b) = (-x, -y)$, $k = 1$, and $c = -(8x + 8x^3 + 3xy^2 + 5x^3y^2)/(x(1 - x^2)(y^2 + 2))$, the solution to the reaction-free equation of (15) was exactly

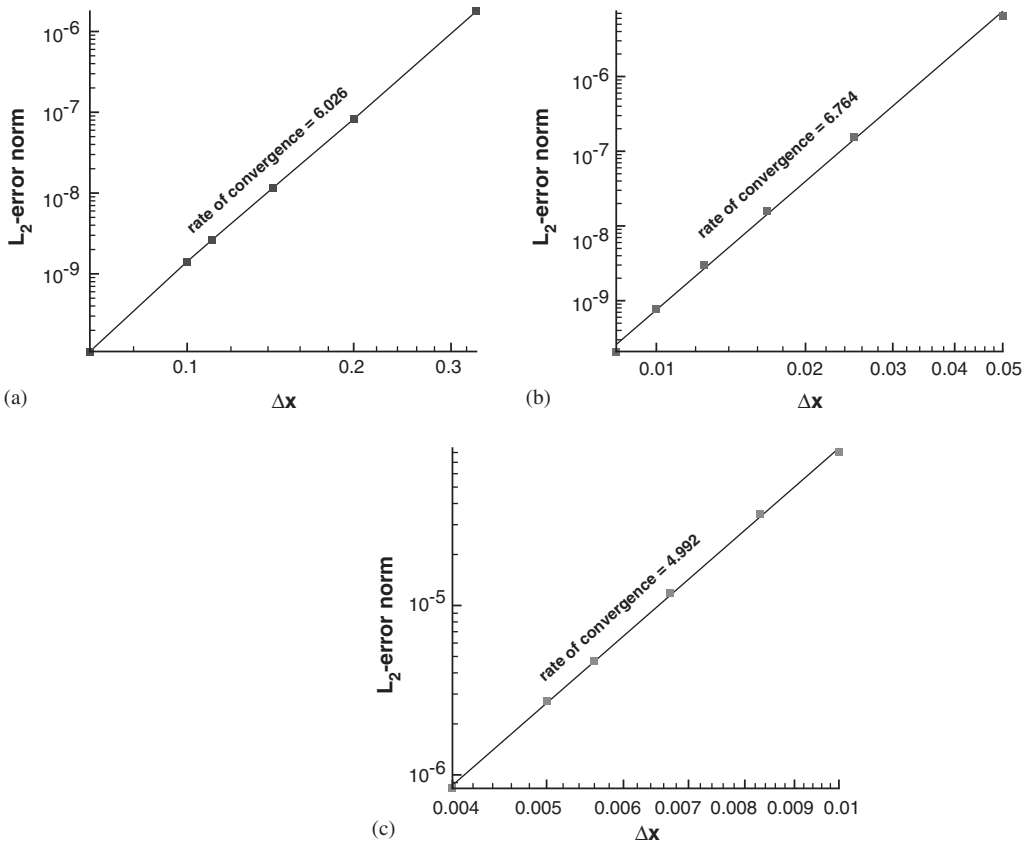

Figure 3. The computed logarithmic L_2-error norms, $\log(\mathrm{err}_1/\mathrm{err}_2)$, against $\log(h_1/h_2)$ for showing the rates of convergence for the first test problem considered in Section 6: (a) $a=b=1$; (b) $a=b=10$; and (c) $a=b=100$.

derived as

$$\phi(x, y) = x(1-x^2)(y^2+2) \tag{55}$$

As before, calculations were performed to obtain the L_2-error norms for cases computed at uniform grids. The corresponding rates of convergence were then plotted in Figure 4 at different values of a and b.

Having verified that the proposed scheme can be successfully applied to solve the steady-state equation, we will consider the transient equation subject to the initial value given by

$$\phi(x, y, t=0) = \exp\left[-\frac{(\bar{x}-x_c)^2+(\bar{y}-y_c)^2}{2M^2}\right] \tag{56}$$

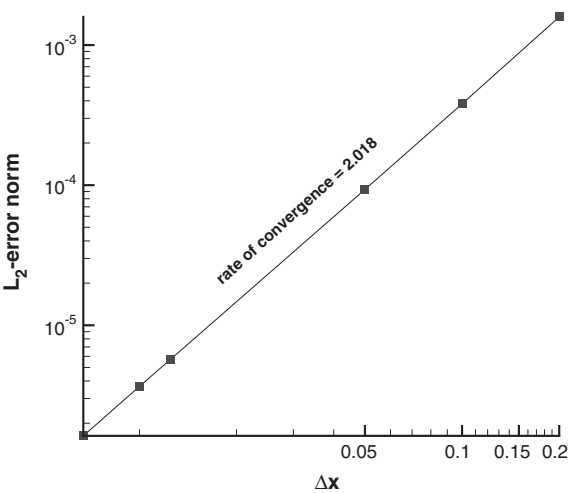

Figure 4. The computed logarithmic L_2-error norms, $\log(\mathrm{err}_1/\mathrm{err}_2)$, against $\log(h_1/h_2)$ for showing the rate of convergence for the second test problem considered in Section 6.

In the unit square domain $-0.5 \leqslant x, y \leqslant 0.5$, the model equation investigated at $(a, b) = (-4y, 4x)$ is amenable to the exact solution given by

$$\phi(x, y, t) = \frac{2M^2}{2M^2 + 4Dt} \exp\left[-\frac{(\bar{x} - x_c)^2 + (\bar{y} - y_c)^2}{2M^2 + 4Dt}\right] \tag{57}$$

where $(\bar{x}, \bar{y}) = (x\cos 4t + y\sin 4t, -x\sin 4t + y\cos 4t)$. Considering that $M^2 = 2 \times 10^{-3}$, $D = 10^{-4}$, $x_c = -0.25$, and $y_c = 0$, the time-evolving values of ϕ are computed at $\Delta t (= 10^{-3})$, $\Delta x = \Delta y (= \frac{1}{64})$ and are plotted in Figure 5. It is clearly seen from these solutions that the simulated contours at $t = 0$, 0.2, 0.4, 0.6, 0.8, 1.0, 1.2, 1.4 and 1.6 retain good symmetry irrespective of the rotating velocity field. As before, calculations were performed to obtain the L_2-error norms at uniform grid sizes and time increments. The corresponding spatial and temporal rates of convergence for the solution computed at $t = \pi/2$ were then plotted in Figure 6 at $\Delta t = 10^{-3}$ and $\Delta x = \Delta y = \frac{1}{64}$, respectively.

To show that our proposed numerical model has the ability to resolve sharp profile, we consider here the mixing of cold and warm fronts in a square domain $-4 \leqslant x, y \leqslant 4$. Initially, the temperature $\phi(x, y, t)$ is given by

$$\phi(x, y, t = 0) = -\tanh\left(\frac{y}{2}\right) \tag{58}$$

Subsequent to $t = 0$, ϕ varies with time in the rotating velocity field centred at the origin $(a, b) = (-\bar{T}\frac{y}{r}, \bar{T}\frac{x}{r})$. Here,

$$\bar{T}\left(\equiv \frac{\sec^2(r)\tanh(r)}{\mathbf{max}[\sec^2(r)\tanh(r)]}\right)$$

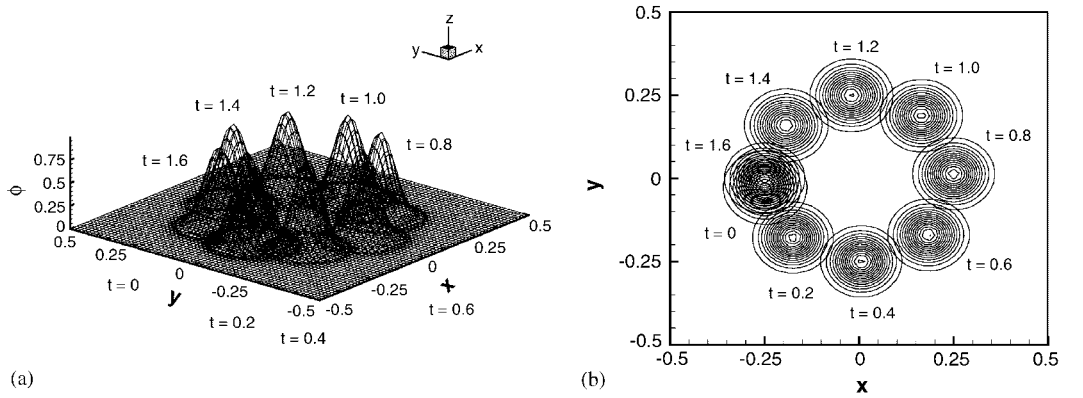

Figure 5. The computed ϕ profiles at different t for the third test problem considered in Section 6: (a) three-dimensional representation of ϕ; and (b) the projection of (a) on the x–y plane.

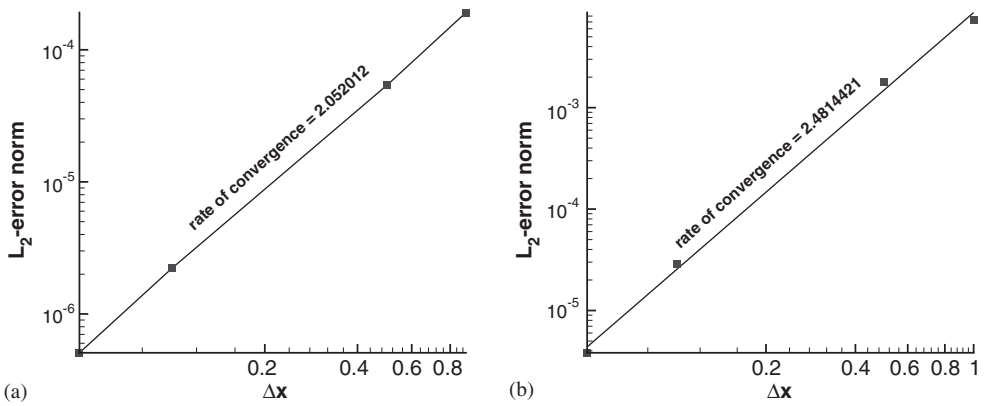

Figure 6. The computed logarithmic L_2-error norms, $\log(\mathrm{err}_1/\mathrm{err}_2)$, against $\log(h_1/h_2)$ for showing: (a) the temporal rate of convergence; and (b) the spatial rate of convergence.

denotes the ratio of the tangential velocity at a location, which is distant from $(0,0)$ with a length of r, and its maximum velocity.

Figure 7 shows the simulated solution $\phi(x, y, t = 4.0)$ for Equation (15) at $c = 0$, $k = 10^{-9}$ and $\Delta x = \Delta y = 0.05$. Due to the rotating velocity field, there exists a marked change in temperature across the interface of the warm and cold fluids. Clearly seen from Figure 7 is that the solid lines advance towards the upper zone. The rotating flow distorts the initially sharp temperature profile and gradually shows a spiral temperature profile. For the sake of comparison, we plot also in Figure 7 the exact solution at the limiting case ($k = 0$) [16]

$$\phi(x, y, t) = -\tanh\left[\frac{y}{2}\cos\omega t - \frac{x}{2}\sin\omega t\right] \tag{59}$$

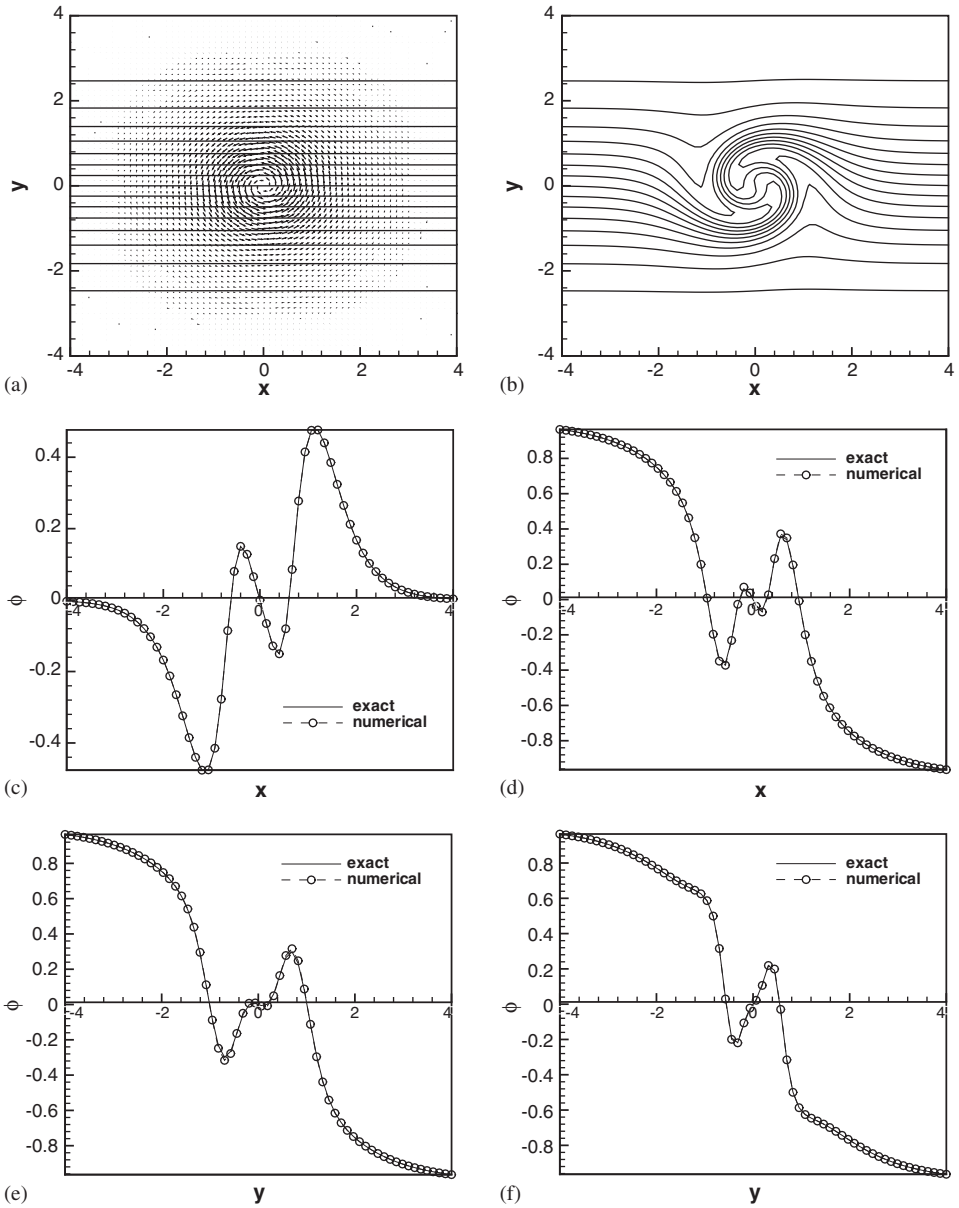

Figure 7. The computed solutions for the mixing of warm and cold fluids: (a) initial condition; (b) exact contours of ϕ for the inviscid case; (c) solution plotted along $\theta = 0^\circ$; (d) solution plotted along $\theta = 45^\circ$; (e) solution plotted along $\theta = 90^\circ$; and (f) solution plotted along $\theta = 135^\circ$.

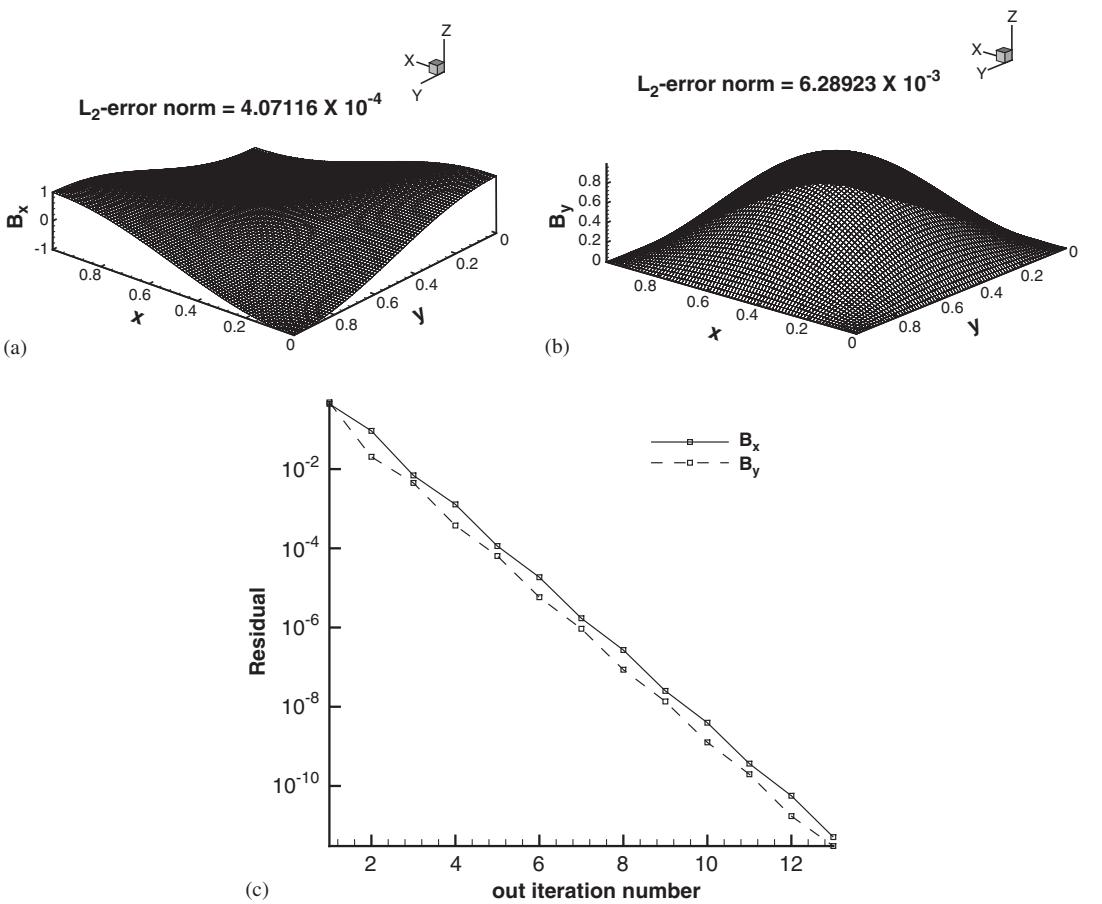

Figure 8. (a) The three-dimensional plot of B_x computed at $\Delta x = \Delta y = \frac{1}{80}$; (b) the three-dimensional plot of B_y computed at $\Delta x = \Delta y = \frac{1}{80}$; and (c) the error reduction plots for B_x and B_y.

In the above, $\omega = \bar{T}/r$ denotes the rotation frequency. The agreement between the simulated and exact solutions is almost entirely satisfactory.

To demonstrate that the proposed scheme can be applied to solve the magnetic induction equations (13) and (14), we have tactically solved equations (10)–(12) in the following divergence-free magnetic field:

$$\mathbf{B} = (B_x, B_y) = (\cos(\pi x)\cos(\pi y), \sin(\pi x)\sin(\pi y)) \tag{60}$$

Solutions to Equations (10)–(12) are those of [17]

$$u = 1 - \mathrm{e}^{\lambda x}\cos(2\pi y) \tag{61}$$

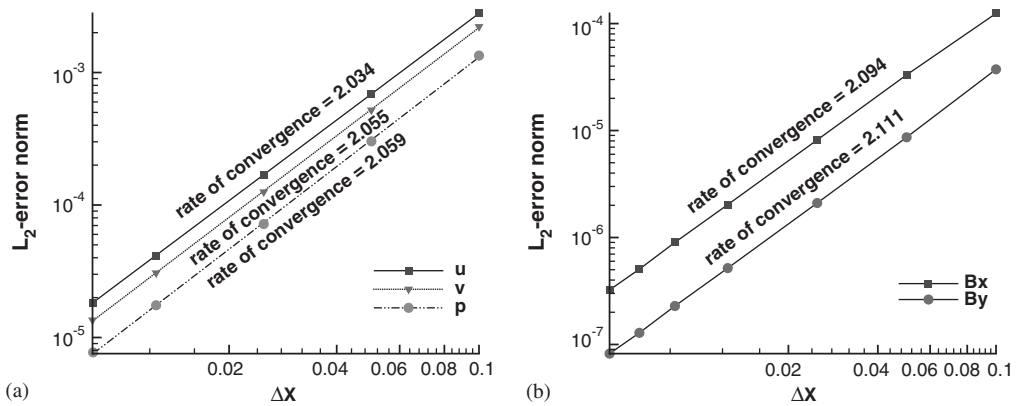

Figure 9. The rates of convergence for: (a) Navier–Stokes equations; and (b) magnetic induction equations.

$$v = \frac{\lambda}{2\pi} e^{\lambda x} \sin(2\pi y) \tag{62}$$

$$p = \frac{1}{2}(1 - e^{2\lambda x}) \tag{63}$$

where $\lambda = Re_f/2 - ((Re_f^2/4) + 4\pi^2)^{1/2}$. The validity of Equations (60)–(63) is subject to the following externally applied source terms:

$$f_1 = e^{\lambda x}\cos(2\pi y)\cos(\pi y)[\lambda\cos(\pi x) + \pi\sin(\pi x)] + \frac{2\pi^2}{Re_m}\cos(\pi x)\cos(\pi y)$$
$$- e^{\lambda x}\sin(2\pi y)\sin(\pi y)\left[\frac{\lambda}{2}\cos(\pi x) + 2\pi\sin(\pi x)\right] - \pi\sin(\pi x)\cos(\pi y) \tag{64}$$

$$f_2 = \frac{\lambda e^{\lambda x}}{2}\sin(2\pi y)\cos(\pi y)\left[\sin(\pi x) + \frac{\lambda}{\pi}\cos(\pi x)\right] + \frac{2\pi^2}{Re_m}\sin(\pi x)\sin(\pi y)$$
$$- e^{\lambda x}\cos(2\pi y)\sin(\pi y)[\pi\cos(\pi x) + \lambda\sin(\pi x)] - \pi\cos(\pi x)\sin(\pi y) \tag{65}$$

The solutions of B_x and B_y for the case with $Re_f = 4\sqrt{3\pi}$ and $Re_m = 10$ were obtained iteratively using the proposed scheme.

The computed magnetic field is plotted against x and y in Figure 8. The simulated results agree well with the theoretical results. Since the magnetic field is smoothly distributed, the rate

of convergence is obtained from the computed L_2-error norms in a square domain spanned by $N \times N$ nodes, where $N = 10$, 20, 30, 40, 50, 60. As Figure 9 shows, the rates of convergence for all field variables are about 2. The abscissa is $\log(h_1/h_2)$ and the ordinate is the computed value of $\log(\mathrm{err}_1/\mathrm{err}_2)$.

7. NUMERICAL RESULTS

In the Hartmann–Poiseuille problem [1], a liquid metal having the magnetic permeability $\bar{\mu} = 1.68 \times 10^{-7}$ H/m, electric conductivity $\sigma = 7.14 \times 10^5\ 1/(\Omega - \mathrm{m})$ and kinematic viscosity $\nu_\mathrm{f} = 1.5 \times 10^{-4}$ kg/m s is considered in an infinitely long rectangular duct with a sectional area of $2L \times 2L$, where $L = 0.5$ m. This liquid metal motion is investigated subject to the streamwise pressure gradient $\Gamma(\equiv \partial p/\partial x) = -4.85 \times 10^{-5}$ Pa/m and the fixed magnetic field B_0 in the channel-height direction. Along the perfectly insulated no-slip walls $y = \pm L$, it is plausible to set $v = 0$ and $B_y = B_0$. The resulting equations governing $u(y)$ and $B_x(y)$ are as follows:

$$-\frac{\partial p}{\partial x} + \frac{1}{Re_\mathrm{f}} \frac{\partial^2 u}{\partial y^2} + \frac{H_a^2}{Re_\mathrm{f} Re_\mathrm{m}} B_y \frac{\partial B_x}{\partial y} = 0 \tag{66}$$

$$\frac{1}{Re_\mathrm{m}} \frac{\partial^2 B_x}{\partial y^2} + \frac{\partial u}{\partial y} B_y = 0 \tag{67}$$

Note that the validity of Equation (66) is subject to the divergence-free constraint conditions $\nabla \cdot \mathbf{u} = 0$ and $\nabla \cdot \mathbf{B} = 0$. Given the boundary conditions $u(y = \pm L) = 0$ and $B_x(y = \pm L) = 0$, Equations (66) and (67) can be shown to have the following dimensionless solutions [18, 19]:

$$u(y) = -\frac{Re_\mathrm{f}}{H_a} \frac{\Gamma L}{\rho u_\infty^2} \frac{\cosh(H_a) - \cosh(H_a y)}{\sinh(H_a)} \tag{68}$$

$$B_x(y) = -\frac{Re_\mathrm{m}}{H_a} \frac{\sinh(H_a y) - y \sinh(H_a)}{\cosh(H_a) - 1} \tag{69}$$

Given the liquid metal properties (σ and μ), the pressure gradient Γ, the Hartmann number H_a and the magnetic Reynolds number Re_m, we can obtain B_0 from

$$B_0 = \left(-\frac{L\bar{\mu}\Gamma H_a \cosh H_a}{Re_\mathrm{m} \sinh H_a} \right)^{1/2} \tag{70}$$

Upon obtaining B_0, we can calculate the characteristic velocity $u(y = 0)(\equiv Re_\mathrm{m}/L\sigma\bar{\mu})$ and, then, the dimensionless parameter $\bar{P}(\equiv H_a^2/Re_\mathrm{f}\, Re_\mathrm{m} = N/Re_\mathrm{m})$, which is used to represent the

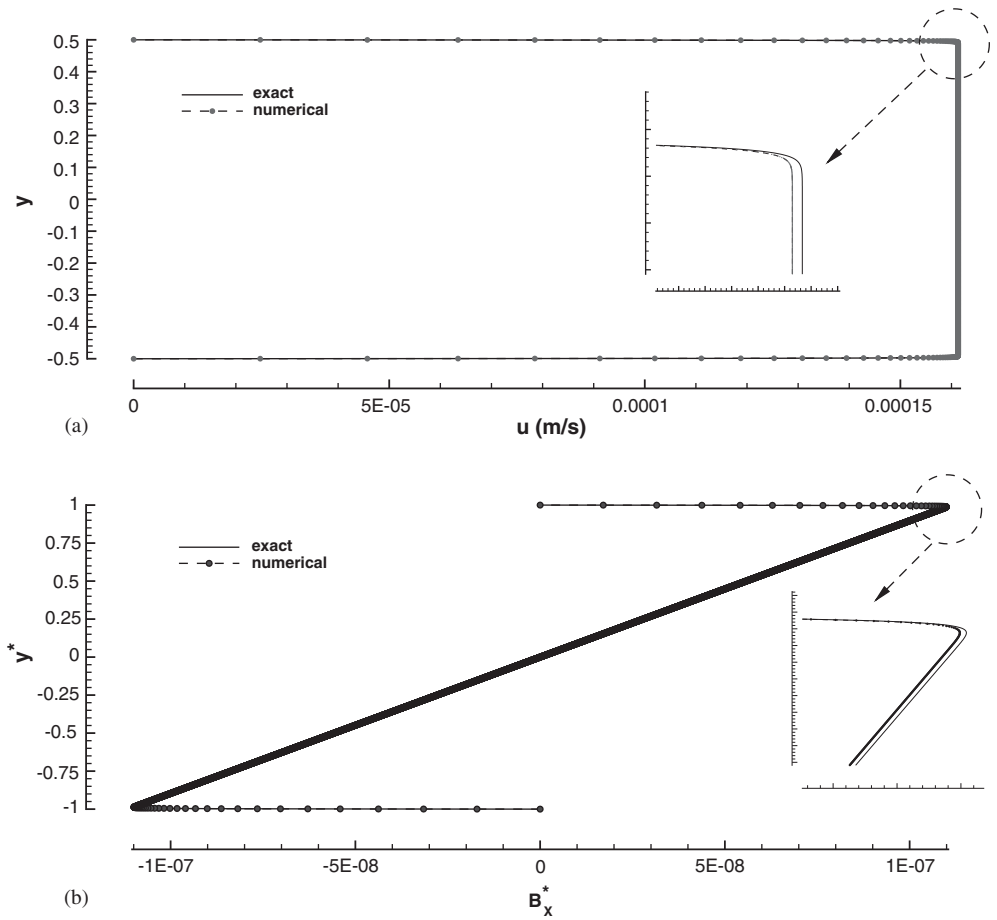

Figure 10. A comparison of the simulated and exact solutions for the case considered at $H_a = 500$: (a) the velocity $u(y)$; and (b) the dimensionless magnetic flux density $B_x(y)^*$.

ratio of the magnetic pressure and the fluid pressure $\frac{1}{2}\rho u_\infty^2$, to close the Hartmann–Poiseuille problem. Here, the interaction number $N(\equiv \sigma L B_0^2/\rho u_\infty)$ (or Stuart number) represents the ratio of Lorentz and inertia forces. All calculations have been carried out at the constant mesh sizes for obtaining grid-independent solutions at each Hartmann number $H_a(\equiv \sqrt{\sigma/\rho\nu_f}B_0 L)$. The results obtained from $H_a = 0$, 1, 5, 10, 50, 100, and 500 are compared with the analytic solutions given in Equations (68) and (69). Take the highest Hartmann number case as an example; the agreement between the simulated and exact solutions for $u(y)$ and $B_x(y)$ is excellent (Figure 10). Upon obtaining the value of $\mathbf{B}$, we can calculate the conduction current density $\mathbf{J} = (J_x, 0)$ from Equation (3) and, then, the electric field $\mathbf{E} = \mathbf{J}/\sigma = (E_x, 0)$. This is followed by calculating the Lorentz forces L_x and L_y in each spatial direction. Here, we plot $J_x, E_x, (L_x, L_y)$ in Figures 11–13, respectively, against y. The analytic solutions are also plotted for the sake of comparison.

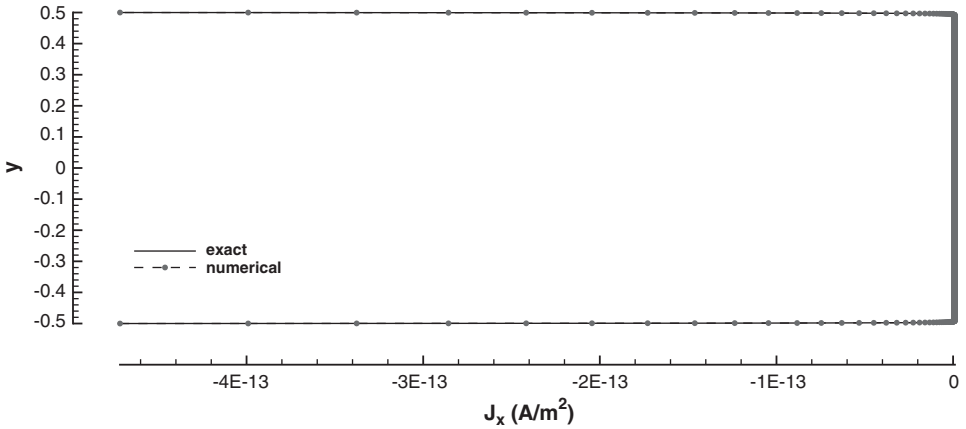

Figure 11. The computed conduction current density $\mathbf{J}(J_x, 0)$ for the case considered at $H_a = 500$.

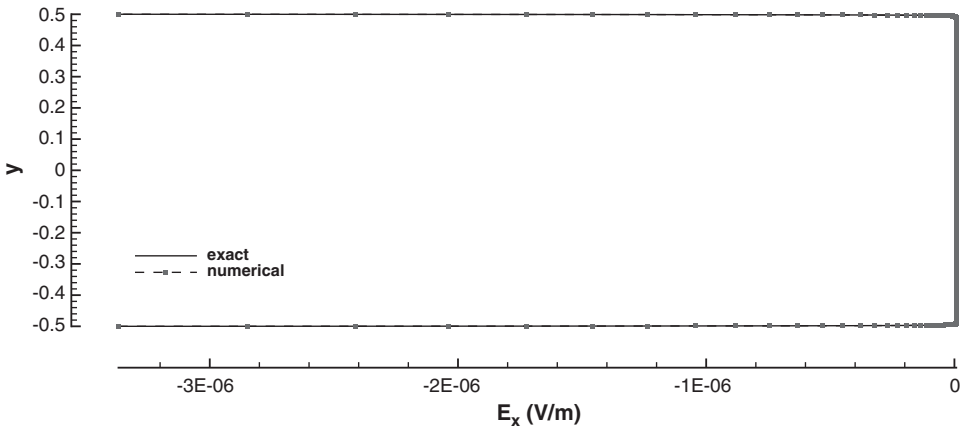

Figure 12. The computed electric field $\mathbf{E}(E_x, 0)$ for the case considered at $H_a = 500$.

We also plot $u(y)$ and $B_x(y)$ at different Hartmann numbers. Apparently seen from Figures 14–17 is that the applied transverse magnetic intensity can indeed affect the flow and magnetic fields. On the increase of H_a, it can be seen from Figure 14 that the simulated velocity profiles become increasingly flattened in the approach to $H_a = 100$. Under these circumstances, a large value of $\partial u/\partial y$ is seen in the so-called Hartmann layer. The larger value of H_a, the thinner the Hartmann layer is. At higher values of H_a, the uniform core, seen in Figures 14–17, extends its size accordingly. The explanation for the magnetic braking is given in Figure 18. It is found that the distribution of axial Lorentz force is opposite to that of the viscous force. This

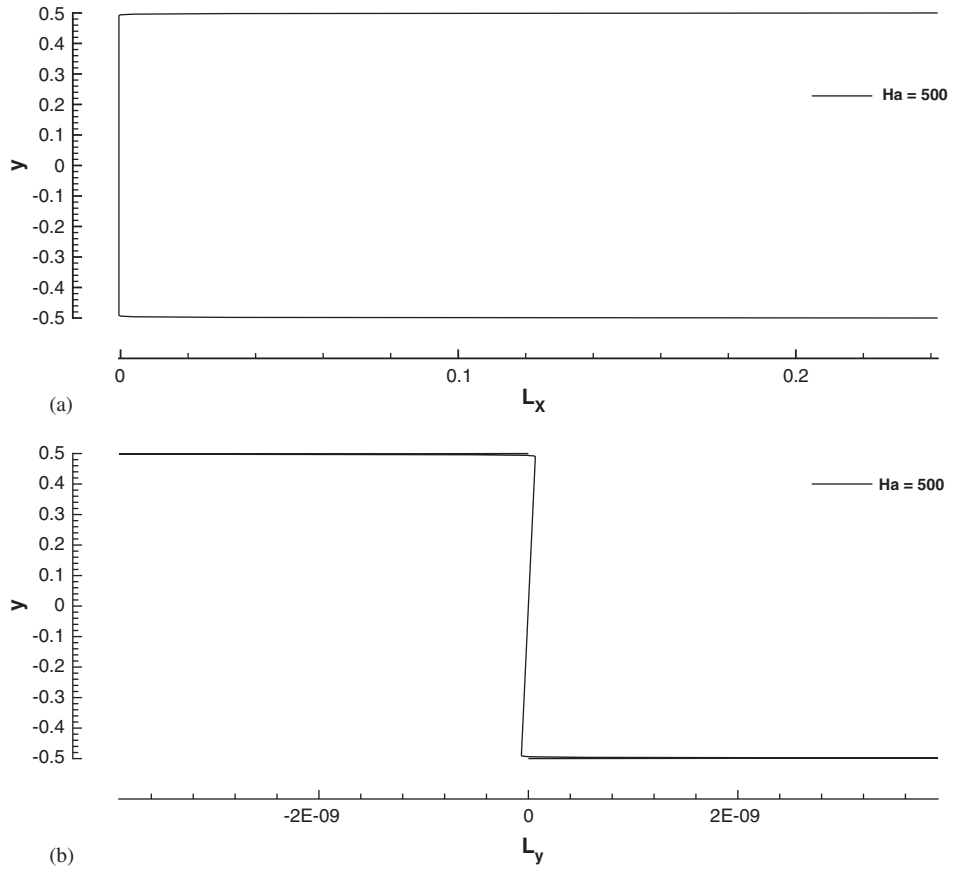

Figure 13. The simulated Lorentz force distributions for the case considered at $H_a = 500$: (a) L_x distribution; and (b) L_y distribution.

counter balance between viscous and Lorentz forces explains the marked difference observed in the ordinary hydrodynamic flow.

8. CONCLUDING REMARKS

A finite-difference method for Navier–Stokes and magnetic induction equations has been developed on non-staggered grids for accurately predicting the high Hartmann-number magnetohydrodynamics. The idea underpinning the present method is the nodally exact one-dimensional constant-coefficient CDR transport scheme applied in each ADI spatial sweep. Emphasis has been placed on the dispersion analysis of the one-dimensional transport equation. Numerical results that demonstrate the validity of the method have been presented by virtue of the Hartmann–Poiseuille benchmark problem.

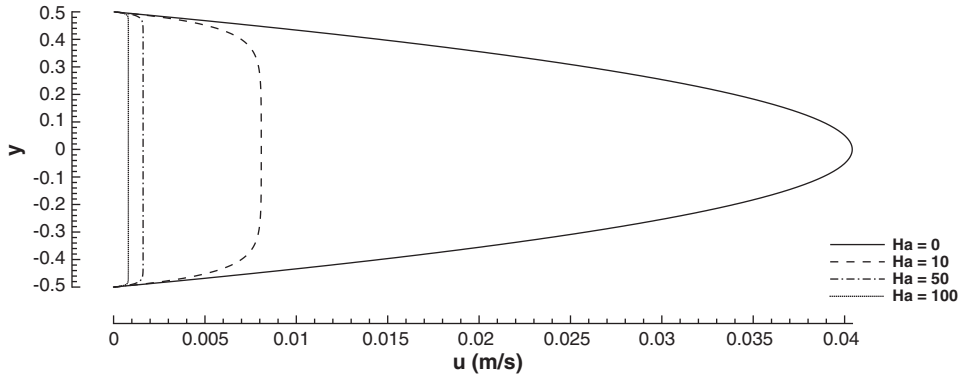

Figure 14. The height-dependent velocities $u(y)$ obtained at different Hartmann numbers.

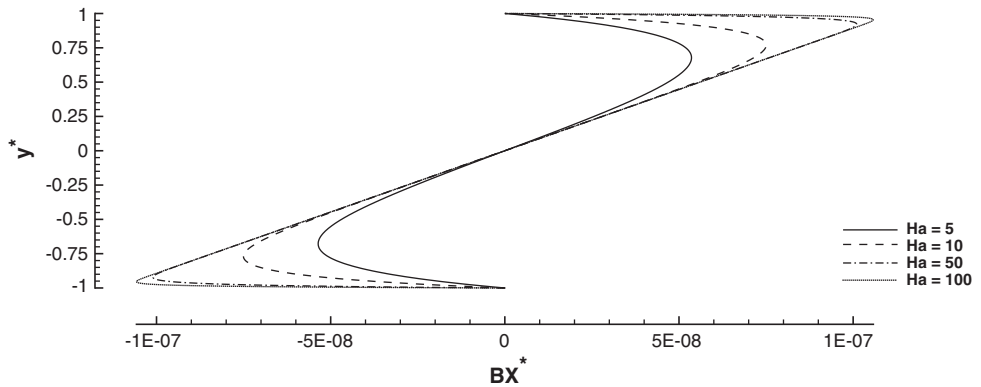

Figure 15. The computed magnetic field $B_x(y)^*$ at different Hartmann numbers.

APPENDIX A

F_1 and F_2 shown in (43) and (44) are expressed below in terms of B_1–B_8,

$$F_1 = B_1 \cos 4\alpha + B_2 \cos 3\alpha + B_3 \cos 2\alpha + B_4 \cos \alpha + B_5 + B_6 \cos \alpha + B_7 \cos 2\alpha + B_8 \cos 3\alpha \quad \text{(A1)}$$

$$F_2 = -(B_1 \sin 4\alpha + B_2 \sin 3\alpha + B_3 \sin 2\alpha + B_4 \sin \alpha - B_6 \sin \alpha - B_7 \sin 2\alpha - B_8 \sin 3\alpha) \quad \text{(A2)}$$

where

$$B_1 = -\frac{1}{60} v \quad \text{(A3)}$$

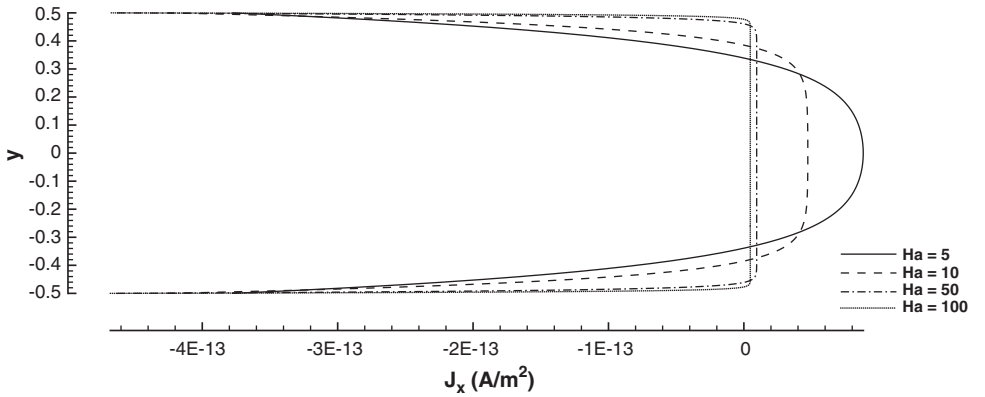

Figure 16. The computed conduction current density field $\mathbf{J}(J_x, 0)$ at different Hartmann numbers.

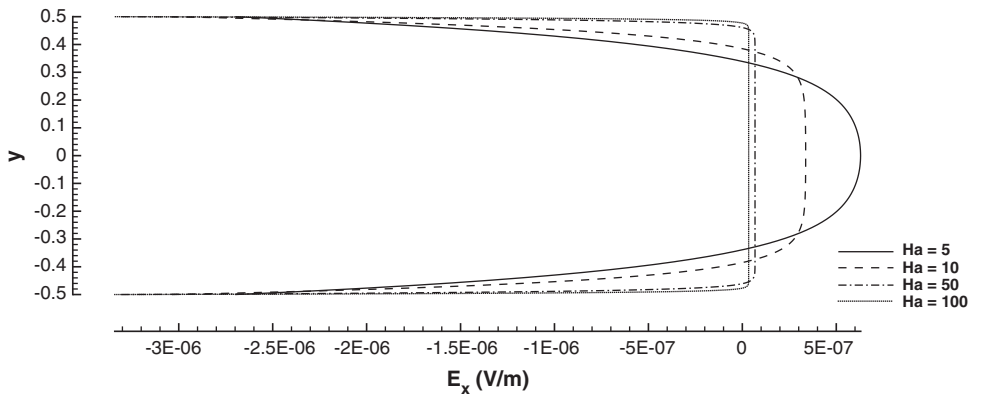

Figure 17. The computed electric field $\mathbf{E}(E_x, 0)$ at different Hartmann numbers.

$$B_2 = \frac{8}{60} v + \frac{2}{180} \frac{v}{Pe} \tag{A4}$$

$$B_3 = -\frac{20}{60} v - \frac{27}{180} \frac{v}{Pe} \tag{A5}$$

$$B_4 = \frac{80}{60} v + \frac{270}{180} \frac{v}{Pe} \tag{A6}$$

$$B_5 = -\frac{35}{60} v - \frac{490}{180} \frac{v}{Pe} - vR \tag{A7}$$

$$B_6 = -\frac{24}{60} v + \frac{270}{180} \frac{v}{Pe} \tag{A8}$$

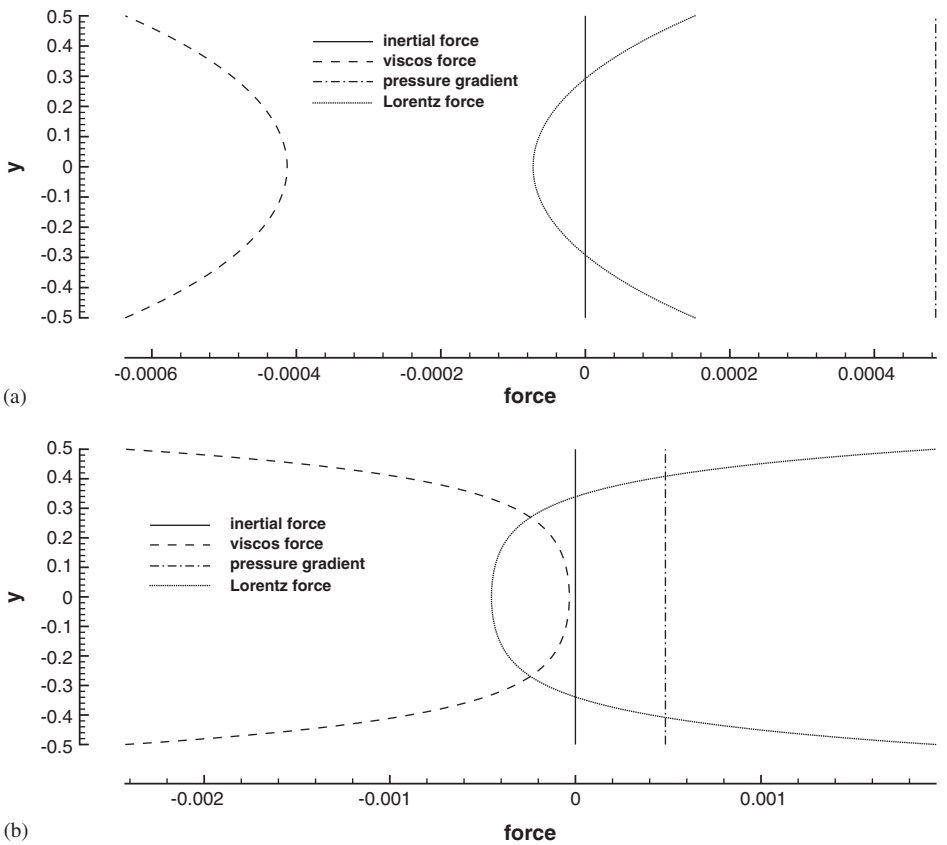

Figure 18. The computed profiles for the Lorentz, viscous, and inertial forces at different Hartmann numbers: (a) $H_a = 1$; and (b) $H_a = 5$.

$$B_7 = \frac{2}{60} v - \frac{27}{180} \frac{v}{Pe} \tag{A9}$$

$$B_8 = \frac{2}{180} \frac{v}{Pe} \tag{A10}$$

ACKNOWLEDGEMENTS

This work was supported by the National Science Council of the Republic of China under Grant NSC 88-2611-E-002-025. I would like to thank one of the reviewers who kindly provided us useful information and reference in the revision of this article.

REFERENCES

1. Moreau R. *Magneto-hydrodynamics*. Kluwer Academic Publishers: Dordrecht, 1990.

2. Strauss HR, Longcope DW. An adaptive finite element method for magnetohydrodynamics. *Journal of Computational Physics* 1998; **147**:318–336.
3. Balsara DS, Spicer D. Maintaining pressure positivity in magnetohydrodynamic simulations. *Journal of Computational Physics* 1999; **148**:133–148.
4. Salah NB, Soulaimani A, Habashi WG, Fortin M. A conservative stabilized finite element method for the magneto-hydrodynamic equations. *International Journal for Numerical Methods in Fluids* 1999; **29**:535–554.
5. Biro O, Preis K. On the use of magnetic vector potential in the finite element analysis of three-dimensional eddy currents. *IEEE Transactions on Magnetics* 1989; **25**:3145–3159.
6. Armero F, Simo JC. Long-term dissipativity of time-stepping algorithms for an abstract evolution equation with applications to the incompressible MHD and Navier–Stokes equations. *Computer Methods in Applied Mechanics and Engineering* 1996; **131**:41–90.
7. Leboucher L. Monotone scheme and boundary conditions for finite volume simulation of magnetodynamic internal flows at high Hartmann number. *Journal of Computational Physics* 1999; **150**:181–198.
8. Hollerbach R, Skinner S. Instabilities of magnetically induced shear layers and jets. *Proceedings of the Royal Society of London A* 2001; **457**:785–802.
9. Peaceman DW, Rachford HH. The numerical solution of parabolic and elliptic differential equations. *Journal of the Society for Industrial and Applied Mathematics* 1955; **3**:28–41.
10. Sheu TWH, Wang SK, Lin RK. An implicit scheme for solving the convection–diffusion-reaction equation in two dimensions. *Journal of Computational Physics* 2000; **164**:123–142.
11. Patankar SV. *Numerical Heat Transfer and Fluid Flow*. Hemisphere: New York, 1990.
12. Harlow FW, Welch JE. Numerical calculation of time-dependent viscous incompressible flow of fluid with free surfaces. *The Physics of Fluids* 1965; **8**:2182–2189.
13. Rhie CM, Chow WL. Numerical study of the turbulent flow past an airfoil with trailing edge separation. *AIAA Journal* 1983; **21**:1525–1532.
14. Ghia U, Ghia KN, Shin CT. High-*Re* solutions for incompressible flow using the Navier–Stokes equations and a multigrid method. *Journal of Computational Physics* 1982; **48**:387–411.
15. Rai MM, Anderson DA. Application of adaptive grids to fluid flow problems with asymptotic solutions. *AIAA Journal* 1982; **20**:496–502.
16. Tamamidis P, Assanis DN. Evaluation for various high-order-accuracy schemes with and without flux limiters. *International Journal for Numerical Methods in Fluids* 1993; **16**:931–948.
17. Kovasznay LIG. Laminar flow behind a two-dimensional grid. *Proceedings of the Cambridge Philosophical Society* 1948; **44**:58–62.
18. Bershader D, Landshoff R. Magnetohydrodynamics. In *Handbook of Fluid Dynamics*, Streeter VL (ed.). McGraw-Hill Book Company, Inc.: New York, 1961; 27-1–27-52.
19. Landau LD, Lifshitz EM, Pitaevskii LP. *Electrodynamics of Continuous Media.* Pergamon Press: Oxford, 1984.

